

The Neutral Gas Properties of Extremely Isolated Early-Type Galaxies III

TRISHA ASHLEY,^{1,2} PAMELA M. MARCUM,² MEHMET ALPASLAN,³ MICHAEL N. FANELLI,² AND JAMES D. FROST¹*Space Telescope Science Institute*²*NASA Ames Research Center*³*New York University*

ABSTRACT

We report on the neutral hydrogen gas content (21-cm emission) of eight extremely isolated early-type galaxies (IEGs) using the Green Bank Telescope. Emission is detected in seven of the eight objects. This paper is the third in a series that collectively present new H I observations for 20 IEGs. Among the 14 H I detections in our observations, eight exhibit a Gaussian-like H I line profile shape, four are double-peaked, one is triple-peaked, and another has a plateaued rectangular shape. Five additional IEGs observed in previous surveys were added to our analysis, bringing the total number of IEGs with H I observations to 25. Of these objects, emission is detected in 19 (76%). The 25 IEGs in our combined study have gas masses that are systematically larger than their luminosity-matched comparison galaxy counterparts. The isolated early-type galaxies presented here follow a trend of increasing gas-richness with bluer B–V colors. This correlation is also observed in a comparison sample drawn from the literature composed of loose group and field early-type galaxies. Two IEGs, KIG164 and KIG870, exhibit properties highly anomalous for spheroidal systems: luminous ($M_B = -20.5, -20.1$) and blue ($B-V = 0.47, 0.48$) respectively, with substantial neutral gas, $M_{HI} = 4.1$ & $5.5 \times 10^9 M_\odot$. Other IEG systems may represent early-type galaxies continuing to assemble via quiescent H I accretion from the cosmic web or relaxed merged systems.

Keywords: galaxies: elliptical and lenticular, cD – galaxies: evolution – galaxies: ISM – galaxies: star formation

1. INTRODUCTION

Early-type galaxy (ETG) formation and evolution is likely to be driven by multiple mergers, a process facilitated in cluster environments in which ETGs preferentially reside. Isolated early-type galaxies (IEGs) present a unique opportunity to test this formation model and to study the nature of ETG evolution outside of the influences of the massive cluster environment e.g., ram pressure stripping, ionizing intraculus-

ter material, tidal harassment, and gas strangulation (Larson et al. 1980; Moore et al. 1999; Gunn & Gott 1972; Lokas et al. 2016). The isolated nature of these systems strongly limits the possible sequences of events leading to their formation with primary mechanisms including early-epoch monolithic collapse or the coalescence of an isolated group of galaxies (Marcum et al. 2004; Niemi et al. 2010; Naab et al. 2007).

ETGs in low density environments are notably bluer and more gas-rich than their cluster ETG counterparts (Huchtmeier et al. 1995; Aars et al. 2001; Marcum et al. 2004; Niemi et al. 2010; Fuse et al. 2012; Ashley et al. 2017, 2018). The bluer colors are suggestive of higher star formation rates over the past ~ 0.5 Gyr (Bruzual & Charlot 2003). Cold gas reservoirs that can be used to fuel star formation in such ETGs are likely to remain unperturbed outside of the dynamically active

tashley@stsci.edu

pamela.m.marcum@nasa.gov

ma5046@nyu.edu

michael.n.fanelli@nasa.gov

jim.frost@gmail.com

cluster environment. Potential origins of gas reservoirs include accretion of surrounding gas clouds and/or recent mergers of nearby companions (Kereš et al. 2005; Macciò et al. 2006). Some isolated ETGs may also still be in the process of forming and have not had sufficient time to ionize, expel, and/or consume a majority of their neutral gas (van Driel & van Woerden 1991; Barnes 2002; Niemi et al. 2010; Serra et al. 2012). While the H I content of field ETGs and correlations with local environment has received increased attention (e.g. Morganti et al. 2006, Oosterloo et al. 2010, Serra et al. 2012), significantly fewer H I studies of *isolated* or void ETGs have been conducted (three in Kreckel et al. (2012), 12 in Ashley et al. 2017, 2018). The Void Galaxy Survey (Kreckel et al. 2012) measured the H I content and kinematics for 60 morphologically diverse systems residing in voids identified in the Sloan Digital Sky Survey, detecting 41 generally H I gas-rich, low-luminosity, blue disk galaxies. None of the three morphologically classified ETGs in their survey was detected in H I. Based on the observed gas kinematics and star formation activity, Kreckel et al. (2012) suggest that the void galaxy population is still in the process of assembling. A number of the Void Galaxy Survey objects have nearby companions and are therefore not necessarily locally isolated system. The highly isolated galaxies presented in this paper allow a study of galaxy gas content to local galaxy number densities even lower than those of general void systems.

H I spectra provide insight into both the kinematics of neutral gas and the fuel available for star formation. These data facilitate understanding of the origin, size, and longevity of the H I reservoirs in highly isolated systems and permit comparison to galaxies evolving in higher density environments. This paper is the third in a series discussing the H I content of extremely isolated early-type galaxies. Two previous papers, Ashley et al. (2017, 2018), hereafter Papers 1 & 2, presented Green Bank Telescope (GBT) H I data for 12 IEGs. This paper presents GBT H I data for eight additional IEGs, accounting for all 20 objects observed by us. Five additional galaxies for which H I data was published by other groups is included in the analysis. This study of 25 isolated objects increases both the number of such systems observed in H I as well as the range in properties of the sample, e.g., luminosity and color, for which H I data exist. Section 2 discusses the IEG and comparison samples. Section 3 presents the observations, data reduction, and measured and derived H I properties. Section 4 reviews the individual H I profiles and compares gas-richness of the IEGs to the comparison sample. Section 5 summarizes the results.

2. SAMPLE SELECTION

2.1. *Isolated Early-type Galaxy Sample*

The sample of extremely isolated early-type galaxies presented here is drawn from the compilations of Marcum et al. (2004) and Fuse et al. (2012) (M04 & F12). An “early-type” morphology was assigned to galaxies with bulge-to-total light ratios (B/T) of ≥ 0.6 (Marcum et al. 2004) or inverse concentration index ratios (R_{50}/R_{90}) of ≤ 0.38 (Fuse et al. 2012), resulting in a dataset including both elliptical and S0 galaxies ($-5 < T \leq -1$). The parent samples were chosen to be separated by at least 2.5 Mpc in co-moving distance from neighboring galaxies brighter than $M_V = -16.5$ (~ 2 magnitudes dimmer than ATLAS 3D), eliminating the possibility of past interactions with any non-dwarf companions (Aars et al. 2001). Using deep optical images, M04 & F12 found evidence of past interactions and mergers in several of the IEGs, including asymmetric outer isophotes and multiple nuclei. The M04 sample was drawn from the Catalog of Isolated Galaxies (Karachentseva 1973) and contains nine IEGs brighter than $M_B < -19.6$ with a range of colors, $0.46 < B-V < 0.96$. The larger F12 sample, extracted from the Sloan Survey, is on average bluer in color, less luminous, and smaller in physical extent than the M04 set, with average values of $B-V = 0.63$, $L_B = 1.13 \times 10^9 M_\odot$, and optical radius of ~ 4.5 kpc. Consistent with the approach adopted for the H I photometry presented in Papers 1 & 2, galaxies predicted to have an H I line flux sufficient to provide a 5σ detection within a ~ 10 -hour exposure were selected as targets. Of the 35 IEGs considered for GBT observations presented here and in Papers 1 & 2, twelve objects were eliminated as viable GBT targets due to large exposure times estimated for a threshold detection.

Basic properties for the IEGs with H I data are given in Table 1. The eight IEGs that are the primary focus of this paper are listed in the upper half of the table. Three of these objects were observed in other H I surveys with two detections: S0926 from early ALFALFA results, (Haynes et al. 2011) and S1110 (Kreckel et al. 2012). S1048 was targeted but not detected by Kreckel et al. (2012). The lower half of the table provides adopted properties for other IEGs having H I data, including observations from Papers 1 & 2 and from previous surveys that covered five IEGs not observed by us (S1221 & S1327, Kreckel et al. (2012); S1323, Most et al. (2013), Mrk737, Salzer et al. (2002), and NGC 1211, Springob et al. (2005)). Unless otherwise noted, these 25 galaxies comprise the “IEG sample” referenced throughout this paper. These objects span a

Table 1. Basic Galaxy Information

Name	Abbrev. Name	RA (2000)	Dec (2000)	Distance	Size	Size	V	M_B	B–V	L_B
		(hh mm ss.s)	(dd mm ss)	(Mpc)	($''$)	kpc	(km s^{-1})	(mag)	(mag)	($10^8 L_\odot$)
(1)	(2)	(3)	(4)	(5)	(6)	(7)	(8)	(9)	(10)	11
KIG164	K164	05 55 03.68	+74 42 52.88	127	33	20.3	9033	−20.5	0.47	234.1
SDSSJ092657.99+100301.4	S0926	09 26 57.98	+10 03 01.40	73	28	9.9	5313	−18.0 ^a	0.24	24.3
SDSSJ094410.80+001047.3	S0944	09 44 10.90	+00 10 47.11	46	26	5.8	3333	−16.5 ^a	0.47	5.9
SDSSJ104807.06+430525.5	S1048	10 48 07.05	+43 05 25.47	58	17	4.8	4005	−15.8 ^a	0.41	3.1
SDSSJ111029.62+134558.1	S1110	11 10 29.61	+13 45 58.12	61	22	6.5	4331	−16.8 ^a	0.44	7.5
KIG684	K684	15 27 14.86	+77 09 24.61	78	50	19.0	5380	−19.5	0.98	91.8
SDSSJ155325.18+520416.5	S1553	15 53 25.18	+52 04 16.50	48	28	6.5	3109	−16.9 ^a	0.47	8.8
SDSSJ212753.52−070113.9	S2127	21 27 53.52	−07 01 13.92	49	38	9.1	3519	−17.9 ^a	0.36	20.8
Basic Information for IEGs Presented in Other Papers										
SDSSJ024248.69−082356.6	S0242	02 42 48.69	−08 23 56.63	58	38	10.7	4337	−17.5 ^a	1.03	14.4
NGC1211	N1211	03 06 52.41	−00 47 40.14	43	92	19.1	3216	−20.2	0.86	174.5
VIII Zw 40	Z40	09 11 05.57	+09 20 58.40	51	26	6.3	3660	−17.4 ^a	0.90	13.2
SDSSJ102145.89+383249.8	S1021	10 21 45.89	+38 32 49.78	60	18	5.3	4204	−17.1 ^a	0.34	10.5
Mrk150	M150	10 38 37.24	+44 31 23.08	54	49	12.9	3700	−18.3	0.35	31.4
SDSSJ113237.43+472658.7	S1132	11 32 37.43	+47 26 58.67	25	21	2.6	1453	−14.2 ^a	0.50	0.7
Mrk737	M737	11 35 23.86	+31 39 15.16	49	31	7.3	3348	−17.2 ^a	0.28	11.8
SDSSJ122123.13+393659.5	S1221	12 21 23.12	+39 36 59.48	65	13	4.2	4482	−15.9 ^a	0.36	3.3
KIG557	K557	12 55 16.57	+00 14 48.81	197	39	37.0	14304	−20.7	1.02	274.2
SDSSJ132337.69+291717.1	S1323	13 23 37.69	+29 17 17.08	59	16	4.6	4068	−15.6 ^b	0.49	2.6
SBS1327+597	S1327	13 27 18.56	+59 30 10.25	72	32	11.3	4956	−18.0 ^a	0.92	24.2
SDSSJ143538.00+435937.1	S1435	14 35 38.00	+43 59 37.10	77	20	7.5	5333	−17.0 ^a	0.46	9.3
KIG792	K792	17 11 51.43	+41 38 57.69	129	47	29.6	9188	−20.4	0.89	209.3
KIG824	K824	17 40 38.03	+41 18 04.62	78	54	20.4	5352	−19.5	0.89	98.4
KIG870	K870	19 11 48.90	+83 54 20.27	89	50	21.7	6197	−20.1	0.48	160.3
SDSSJ234042.69−092336.6	S2340	23 40 42.68	−09 23 36.59	70	30	10.1	5146	−18.2 ^a	0.45	29.1
SDSSJ235021.45+141342.6	S2350	23 50 21.45	+14 13 42.60	72	16	5.4	5142	−15.3 ^b	0.55	2.0

NOTE—Column: (1) Designation taken from the Catalog of Isolated Galaxies (Karachentseva 1973) or the Sloan Digital Sky Survey (Abazajian et al. 2009), respectively. (2) Abbreviated galaxy designation. (3)-(4) Galaxy coordinates sourced from the NASA/IPAC Extragalactic Database (NED). (5) Adopted distances derived from the Virgo Cluster infall corrected recessional velocities as reported in NED. (6) Optical major axis diameter. For the KIG sources, these values come from M04, where they were directly measured from deep imagery; sizes for the rest of the sample are obtained from the diameter measurements listed in NED. (7) Physical major axis diameter derived from Cols. (5) & (6). (8) Heliocentric optical velocities taken from NED. (9)-(10) Absolute B-band magnitude and B-V color. These data are sourced from M04 for the KIG sample. For the others, photometry was obtained from NED where B & V-band exists, else transformed using ugriz magnitudes from the NASA Sloan Atlas. Foreground extinction corrections were applied using Schlafly & Finkbeiner (2011). (11) B-band luminosity in solar units computed from Col. (8), using an absolute solar luminosity $M_{\odot,B} = 5.44$ mag (Willmer 2018).

^a Photometry derived through transformation of NSA Sersic flux data; see Section 3.1 for details.

^b S2350 not in the NSA; transformed NSA photometry produced unphysical B–V color for S1323. Photometry derived instead through transformation of SDSS Cmodel values using same prescription as for NSA-derived values.

factor of 400 in luminosity ($-14.2 < M_B < -20.7$) and are generally blue (average $B-V = 0.58$). Exceptions include KIG684, KIG557, SBS1327+597, KIG792 and KIG824 which have red optical colors ($B - V \gtrsim 0.9$) typical of luminous elliptical galaxies.

2.2. Comparison Galaxy Sample

To place our highly isolated systems in an evolutionary context, the H I properties of the IEGs are compared to those of 86 ETGs drawn from Huchtmeier et al. (1995), Grossi et al. (2009) and Serra et al. (2012, 2008) (hereafter, the “comparison” sample). Data in this comparison sample include both single dish and interferometric observations. Galaxies with known cluster membership (e.g., NGC4406, NGC4472 and NGC4694) were excluded from the comparison sample, as were dwarf companions to large galaxies such as NGC185 and NGC205. Also excluded were galaxies associated with compact groups. The intent of these exclusions is to construct a comparison sample consisting of “field” and loose group galaxies. With the exception of the IEG galaxies, the comparison galaxies serve as the lowest density environment sample with published H I data. A published H I observation for another galaxy, NGC7465, was removed because the beam included gas from other group members. All other H I-detected ETGs from these four references were included. Duplication was eliminated by using data from the source having the most recent publication date. Over 90% of these galaxies are catalogued group members. The remaining $\sim 10\%$ have no apparent catalogued group/cluster affiliation and are considered to be “field” galaxies. A search of their environments using NED¹ reveals that most of the field galaxies have nearest-neighbors within 0.5 Mpc. The IEGs differ dramatically from the comparison galaxies with respect to degree of isolation. Only one field galaxy in the comparison sample, NGC6798 (Serra et al. 2012), appears to have a low-density environment comparable to the IEGs. Table A1 lists the optical and H I properties for the comparison sample (see Appendix A).

3. OBSERVATIONS AND DATA REDUCTION

3.1. Data Standardization

Properties including optical photometry and distances for both the IEG and comparison samples were extracted from several different published surveys and required standardization. Distances were Virgo In-

fall corrected assuming the following adopted parameters: $H_0 = 73.0$, $\Omega_{\text{matter}} = 0.27$, $\Omega_{\text{vacuum}} = 0.73$. The B -band photometry and $B-V$ colors were adopted in the following order of availability: our own ground-based data (Marcum et al. 2004), B_T (RC3), m_B (RC3), or photometry derived from ugriz fluxes of 2-D Sersic model fits (specifically, the NMGY photometry) taken from the NASA-Sloan Atlas (<http://www.nsatlas.org/>, hereafter “NSA”) and transformed to the Johnson filter system using the prescription of Cook et al. (2014). Optical photometry is extinction-corrected using Schlafly & Finkbeiner (2011). Tables 1 and A1 indicate photometry transformed from the NSA.

Values for H I fluxes for the comparison sample, when directly provided by the source, were used to derive H I masses. If only H I masses were given in a paper, then associated H I fluxes were inferred using distances adopted by the reference.

3.2. H I Observations

H I observations were made using the 100m Robert Byrd Green Bank Telescope from October through December 2017. The GBT provides a $9'$ beam which is sufficiently sized to detect emission from neutral gas reservoirs within or surrounding the IEG sample. Using the L-band receiver and VEGAS backend, position-switched single pointing H I observations were made over a bandwidth of 16.875 MHz. Calibrators were chosen from the GBT calibrator catalog during the beginning of each observing run and were used to point and focus the telescope.

Standard data reduction techniques were used to calibrate the data using GBTIDL². The data (with an original channel width of 0.22 km s^{-1}) were Hanning smoothed and the procedure GETPS was used to calibrate the antenna temperature of the data. RFI spikes were identified and manually removed by interpolating over neighboring channels. Boxcar smoothing over three channels was performed to increase the signal-to-noise ratio of the line profiles. Polynomials of 3rd-7th order were then fit to the baselines in order to remove environmental and instrumental effects. Finally, the data were smoothed using a boxcar function over five channels resulting in a final channel width of $\sim 6.9 \text{ km s}^{-1}$.

The GBTIDL procedure STATS was used to derive an estimate of the H I mass and root-mean-square (rms) uncertainty for each galaxy. The noise rms was calculated using emission-free baseline-subtracted channels. The STATS procedure is used to measure the area under

¹ The NASA/IPAC Extragalactic Database (NED) is operated by the Jet Propulsion Laboratory, California Institute of Technology, under contract with the National Aeronautics and Space Administration.

² Developed by NRAO; for documentation see <http://gbtidl.nrao.edu/>.

the curve of any emission in the line profiles, a value equal to the sum of flux (S) over N channels times the channel width. This integrated flux density is used in the following equation to calculate an H I mass:

$$M_{\text{HI}}(M_{\odot}) = 2.356 \times 10^5 D^2 \sum_i S_i \Delta V \quad (1)$$

where D is the distance of the galaxy in Mpc, S_i is the flux in the i^{th} channel in Jy, and ΔV is the channel width in km s^{-1} .

Table 2 provides information associated with the H I observations, measured values, and derived values for each IEG (the upper half contains the most recent observations, the lower half contains observations from the literature³). Upper limits for H I masses are calculated by setting the H I flux density to five times the rms per channel (σ_{rms}), assuming that the emission is spread over 100 km s^{-1} (a number that is easy to adjust and a reasonable velocity width for ETGs: Huchtmeier et al. 1995; Grossi et al. 2009):

$$M_{\text{HI}}(\text{upper}) = 2.356 \times 10^5 D^2 (5\sigma_{\text{rms}} \times \frac{100}{\sqrt{N}}). \quad (2)$$

where N is the number of channels spanning 100 km s^{-1} . Figure 1 presents the H I line profiles of the IEG sample.

4. RESULTS AND DISCUSSION

4.1. Individual Galaxies

Four of the H I spectra shown in Figure 1 show single-peaked Gaussian-like shaped profiles. Two galaxies exhibit asymmetric emission around the line centroid and one shows a steep-sided rectangular shape, similar to the double-horned profile typical of rotating disk systems but lacking the central deficit of emission which produces the ‘‘horns.’’ Although a unique determination of the H I gas distribution is not possible using just the single dish spectrum, the shape of the profile can be used to obtain information about the global gas content and gas kinematics.

A number of plausible 3D H I distributions may produce the observed spectral shapes. Gaussian-like profiles may indicate that the H I has little rotational support or is contained in a low-inclination disk with little line-of-sight velocity spread. Lower luminosity systems may possess dwarf-like disks with near solid body rotation and a high central gas density producing a Gaussian-like profile. Serra et al. (2012) found that roughly two-

thirds of their ETG sample detected in H I (64%) have rotating H I discs or rings. Since their sample consisted of luminous ETGs, we would expect that our more luminous systems also contain a significant fraction of rotating disks. For most of our IEGs, the emission velocity widths displayed in Figure 1 are sufficiently large which could be the result of substantial rotational support. Profiles may also be broadened and exhibit asymmetries due to tidally (merger) induced dynamic perturbations, producing both infalling and outflowing clouds. Both gas-rich KIGs in our sample show optical-band distortions in their 2D light profiles (Marcum et al. 2004), strongly suggesting that these systems have accreted gas from a past merger. Finally, while these systems are all isolated from nearby massive companions, faint H I-rich dwarf companions or circumgalactic material lying within the 9' GBT beam could contribute to profile asymmetry.

Below we briefly discuss each system, more profile analysis will be presented in Paper IV.

KIG164 (Figure 1a) shows strong asymmetric emission with two peaks having amplitudes reaching 14σ and 9σ , respectively. The optical systemic velocity falls directly within the dip in amplitude between the two peaks. The profile suggests that more gas is blueshifted with respect to the systemic optical velocity than is redshifted. KIG164 possesses the second largest H I mass in the larger 25 IEG sample of this work with $M_{\text{HI}}=4.7 \times 10^9 M_{\odot}$, only surpassed by KIG870 which has an H I mass of $5.8 \times 10^9 M_{\odot}$. This H I mass is also large relative to that of the ETG samples of Grossi et al. (2009) and Serra et al. (2012). Only two galaxies in those studies have larger H I masses: UGC4599 and NGC7465 with H I masses of $7.6 \times 10^9 M_{\odot}$ and $9.5 \times 10^9 M_{\odot}$, respectively. Galaxies in the Huchtmeier et al. (1995) sample have larger H I masses than that of Grossi and Serra, with six galaxies containing H I masses greater than that of KIG164 (M_{HI} of $5.3 - 18.7 \times 10^9 M_{\odot}$).

Although the H I profile displays two peaks, the profile’s asymmetry, and narrow and shallow dip together do not match the expected characteristics of a rotating disk with a double-horn profile. Using deep optical imagery Marcum et al. (2004) found low-level features indicative of an advanced merger, including a morphologically asymmetric nucleus and a potential stellar bridge between KIG164 and a possible dwarf companion. KIG164’s H I line profile could indicate that the

³ Note that some H I and photometric values for galaxies from Papers 1 & 2 may be slightly different from their previously-published values due to differences in adopted distances.

Table 2. GBT Observations

Name	T_{source}	Physical Beam	rms	S_{HI}	ΔV	M_{HI}	$\log_{10}(M_{HI}/L_B)$	H I Source
	(hr)	(kpc)	(mJy)	(Jy km s ⁻¹)	(km s ⁻¹)	(10 ⁸ M _⊙)	(M _⊙ /L _⊙)	
(1)	(2)	(3)	(4)	(5)	(6)	(7)	(8)	(9)
KIG164	2.0	333	0.64	1.13 ± 0.03	340	43 ± 1	-0.74	1
SDSSJ092657.99+100301.4	3.9	191	0.49	1.83 ± 0.02	200	23.0 ± 0.2	-0.02	1
SDSSJ094410.80+001047.3	3.5	120	0.51	0.35 ± 0.02	145	1.7 ± 0.1	-0.53	1
SDSSJ104807.06+430525.5	4.5	152	0.49	0.62 ± 0.02	290	4.9 ± 0.2	+0.20	1
SDSSJ111029.62+134558.1	4.5	159	0.38	0.39 ± 0.01	160	3.4 ± 0.1	-0.34	1
KIG684	5.6	205	0.41	≤0.05	...	≤0.8	≤-2.08	1
SDSSJ155325.18+520416.5	2.0	125	0.60	0.66 ± 0.02	200	3.5 ± 0.1	-0.40	1
SDSSJ212753.52-070113.9	2.0	129	0.65	1.90 ± 0.02	190	10.9 ± 0.1	-0.28	1
IEGs HI Data Presented in Other Papers								
SDSSJ024248.69-082356.6	9.0	152	0.49	≤0.06	...	≤0.5	≤-1.46	3
NGC1211	...	113	...	14.98	...	65.4	-0.43	7
VIII Zw40	6.0	132	0.86	≤0.11	...	≤0.7	≤-1.29	2
SDSSJ102145.89+383249.8	7.6	158	0.62	0.60 ± 0.03	260	5.1 ± 0.2	-0.32	2
Mrk150	7.5	141	0.65	1.34 ± 0.03	280	9.2 ± 0.2	-0.54	3
SDSSJ113237.43+472658.7	2.5	65	0.99	1.24 ± 0.03	170	1.8 ± 0.0	+0.39	3
Mrk737	...	128	...	1.49	...	8.4	-0.15	6
SDSSJ122123.13+393659.5	...	170	...	0.35	...	3.5	+0.02	4
KIG557	8.6	515	0.78	≤0.10	...	≤9.2	≤-1.47	2
SDSSJ132337.69+291717.1	...	155	...	0.17	...	1.4	-0.28	5
SBS1327+597	...	189	...	2.07	...	25.4	+0.02	4
SDSSJ143538.00+435937.1	11.0	202	0.51	≤0.07	...	≤0.9	≤-1.00	2
KIG792	6.5	339	0.62	≤0.08	...	≤3.2	≤-1.82	2
KIG824	7.5	204	0.51	0.32 ± 0.02	330	4.6 ± 0.3	-1.33	3
KIG870	5.9	234	0.53	2.91 ± 0.03	475	54.8 ± 0.6	-0.47	2
SDSSJ234042.69-092336.6	6.8	184	0.55	0.28 ± 0.02	160	3.3 ± 0.2	-0.95	3
SDSSJ235021.45+141342.6	5.2	187	0.59	1.30 ± 0.02	220	15.7 ± 0.3	+0.90	3

NOTE—Column: (1) Galaxy designation. (2) Total on-source time. (3) The projected 9' FWHM values of the GBT beam at the distances provided in Table 1. (4) Measured rms noise per channel. (5) H I flux density with 1σ uncertainties. Upper limits (5σ) are given for nondetections. (6) Full width at zero intensity of the emission profile, defining the velocity range over which the GBTIDL program STATS was used to obtain an H I integrated flux density. Upper limit H I masses use $\Delta V=100$ km s⁻¹. (7) Derived H I mass with 1σ uncertainties. (8) Log of the H I mass-to-blue luminosity ratio in solar units. (9) Source of H I data: 1– this paper; 2–Ashley et al. (2018); 3–Ashley et al. (2017); 4–Kreckel et al. (2012); 5–Most et al. (2013); 6–Salzer et al. (2002); 7–Springob et al. (2005)

gaseous component of the galaxy is still in the process of kinematically relaxing into a rotating disk following a recent accretion event or an interaction with the dwarf. KIG164 and KIG870 (discussed in Paper 2) are both gas-rich, blue ($B-V = 0.47, 0.48$, respectively) and luminous ($M_B = -20.5, -20.1$, respectively), far removed from the red sequence of luminous ETGs in the galaxy color-magnitude diagram. Both galaxies exhibit subtle photometric evidence (Marcum et al. 2004) for an interaction and have high-mass star formation as measured by their very blue $B-V$ colors.

KIG684 (Figure 1b) has no reliably detected emission at the sensitivity of the data. The spectrum does show potential low-level emission with a plateau centered on ~ 5425 km s⁻¹, close to the galaxy’s optically-defined systemic velocity. Due to the low significance of this feature ($\sim 1.4\sigma$), we regard this galaxy as being a non-detection in H I emission.

SDSSJ0926 (Figure 1c) has very strong emission with a single peak detected with an SNR of 44σ . Haynes et al. (2011) observed this system as part of the Arecibo ALFALFA survey and finds a

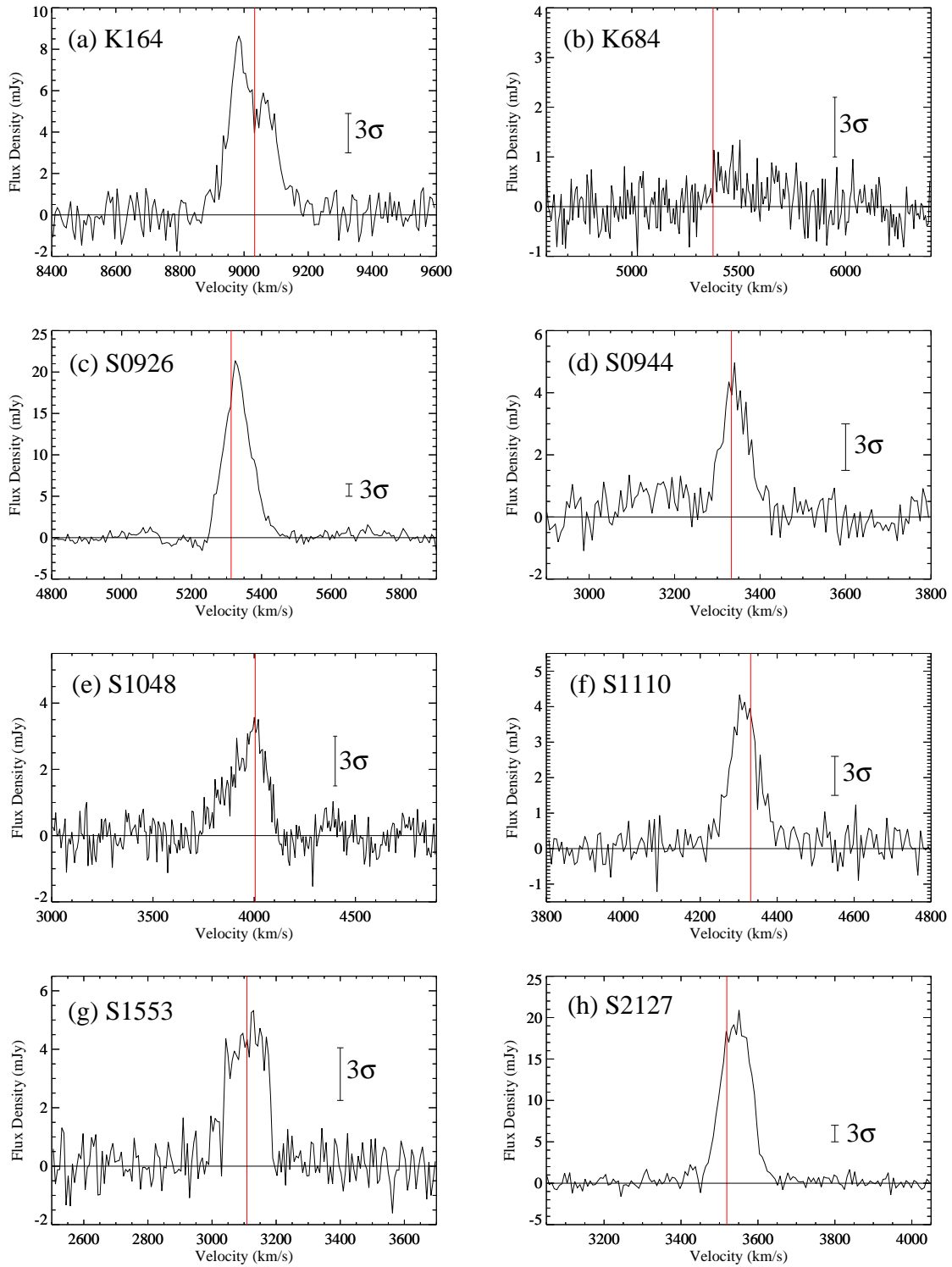


Figure 1. H I line profiles for the 8 IEGs reported here. Source names are given in the upper left corner, shortened for brevity. The red vertical lines indicate the optically defined systemic recession velocity for each galaxy, sourced from NED. Error bar lengths are 3 times the rms per channel. These profiles have been Hanning and boxcar-smoothed resulting in a 6.9 km s^{-1} channel width.

similarly-shaped Gaussian-like profile with an H I centroid at 5334 km s^{-1} , and an integrated flux density $\sim 6.5\%$ larger than ours, consistent with the GBT data. The optical systemic velocity 5313 km s^{-1} ($\pm 2 \text{ km s}^{-1}$) is slightly lower than the velocity of the H I peak at 5325 km s^{-1} . S0926 contains a large H I mass of $2.2 \times 10^9 M_{\odot}$. Fuse et al. (2012) indicate that S0926 may have stellar tidal arms. The H I line profile does not show any obvious signs of this disturbance. The gaseous tidal arms might not show as prominent features in an H I line profile if they are rotating with the disk. Alternatively, the gaseous tidal arms may have changed gas phase (Mihos 2001) or kinematically decoupled from the stellar component (Duc et al. 1997) leaving a residual stellar tidal feature.

SDSSJ0944 (Figure 1d) has a Gaussian-like H I profile shape similar to that of S0926 with a peak emission detected with an SNR of 8σ . The optical systemic velocity and velocity corresponding to the H I line profile centroid are in good agreement. No optically interesting features were noted in Fuse et al. (2012).

SDSSJ1048 (Figure 1e) exhibits an asymmetric Gaussian-like profile with the peak emission having an SNR of $\sim 7\sigma$ and matching well with the optical systemic velocity. S1048's H I line profile is similar in shape to those of S0926 and S0944, however, the shape of the profile is noticeably asymmetric about the optical systemic velocity with a bulk of the emission skewed towards blue-shifted velocities. Fuse et al. (2012) do not identify any optical disturbances in this system that could be associated with the asymmetry in the H I line profile. SDSSJ1048, also designated VGS16, was observed but *not* detected by Kreckel et al. (2012) as part of their Void Galaxy Survey using the Westerbork Synthesis Radio Telescope (WSRT). Their 3σ H I mass upper limit is $1.16 \times 10^8 M_{\odot}$, computed for an assumed profile width of 100 km s^{-1} . This upper limit is consistent with the measured mass provided in Table 2 after taking into account the broad detected profile width ($\sim 290 \text{ km s}^{-1}$).

SDSSJ1110 (Figure 1f) has an emission profile with a Gaussian-like shape. The profile peak has a SNR of $\sim 11\sigma$ and lies at 4310 km s^{-1} compared to the optical systemic velocity of 4331 km s^{-1} ($\pm 25 \text{ km s}^{-1}$). This system was observed by Kreckel et al. (2012) designated VGS19. Using WSRT, they report an H I systemic velocity centroid at 4318 km s^{-1} and an H I mass of

$3.16 \pm 0.76 \times 10^8 M_{\odot}$, consistent with the measurements presented here.

SDSSJ1553 (Figure 1g) has an H I line profile with steep edges and a noisy plateau, giving the profile a rectangular shape. The plateau is detected at an SNR of $\sim 7\sigma$ with the optical systemic velocity falling near the center of the plateau. The rectangular profile could be a shallow double-horned profile that is obscured by the noise. A small second plateau is centered near 3010 km s^{-1} . This second feature was included in the H I mass measurement in Table 2 although it is observed with an SNR of only $\sim 2.3\sigma$. Excluding the emission contribution from this feature, the H I mass decreases from 2.7 to $2.5 \times 10^8 M_{\odot}$.

SDSSJ2127 (Figure 1h) has a Gaussian-like shaped H I line profile similar to those of S0944, S0926, and S1110 with a peak emission having an SNR of 28σ . The profile peak falls at $\sim 3545 \text{ km s}^{-1}$, noticeably higher than the optical systemic velocity of 3519 km s^{-1} ($\pm 5 \text{ km s}^{-1}$).

4.2. Gas Mass-to-Blue Light Ratios

Papers 1 & 2 discuss the relationship between H I mass-to-blue luminosity ratio ($M_{\text{HI}}/L_{\text{B}}$) and optical (B–V) color in ETGs within low-density environments. Figure 2 displays this relationship with our IEG sample shown as green circles. The eight IEGs from this paper are indicated by their abbreviated name. Non-detections are shown as 5σ upper limits. The five IEG galaxies having H I measurements found in the literature (Salzer et al. 2002; Kreckel et al. 2012; Most et al. 2013; Springob et al. 2005) are indicated by dark green circles. Galaxies from the comparison sample are displayed in purple. As noted in Papers 1 & 2, Figure 2 shows that bluer galaxies are generally more gas-rich (higher $M_{\text{HI}}/L_{\text{B}}$) than their red counterparts. We found this relationship to be sufficiently robust to provide predictions of H I flux as the basis of exposure time estimates for GBT observations of the IEGs, most of which had not previously been observed in H I. The solid line in Figure 2, a linear fit to all of the data excluding upper limits, is given as:

$$\log(M_{\text{HI}}/L_{\text{B}}) = -2.3(B - V) + 0.6. \quad (3)$$

Figure 2 illustrates the large range in B–V color for the 25 IEGs: ~ 0.25 to ~ 1.0 . The IEGs fill in the otherwise sparsely-populated blue end of the H I mass/color relationship. The $M_{\text{HI}}/L_{\text{B}}$ for IEGs with detected H I range from $\sim 10^{-4}$ to 8. Of the comparison galaxies, the Grossi sample has characteristics most similar to those

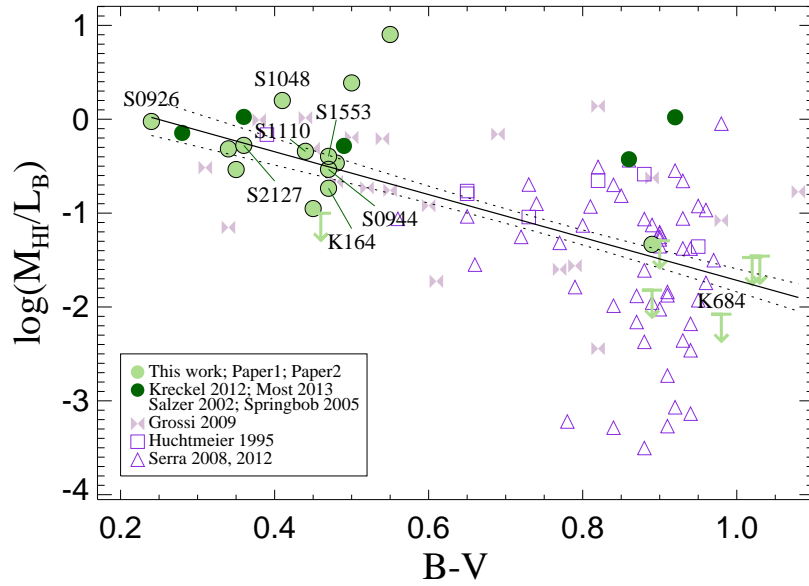


Figure 2. $B-V$ vs. $\log(M_{\text{HI}}/L_B)$ for the entire IEG sample contrasted with the comparison sample. Data presented here and in [Ashley et al. \(2017, 2018\)](#) are shown in filled light green circles. Data for IEGs Mrk737, SDSSJ122123.13+393659.5, SBS1327+597, SDSSJ132337.69+291717.1 and NGC1211 obtained from, respectively [Salzer et al. \(2002\)](#), [Kreckel et al. \(2012\)](#) (2), [Most et al. \(2013\)](#) and [Springbob et al. \(2005\)](#) are displayed in dark green. Data points centered directly under, above or linked to abbreviated galaxy names indicate the 8 new objects presented in this paper. Green arrows represent 5σ upper mass limits for non-detections of IEGs. The comparison ETG sample is shown in purple with the symbol indicating the published source. The linear relationship (black solid line) includes both the detected IEGs and comparison galaxies; dashed lines show the $\pm 1\sigma$ envelop.

of the IEGs; the galaxies in that study are bluer and more dwarf-like in size than other ETGs. The majority of null detections are associated with the redder galaxies. As noted in Paper 2, the IEGs in the red end of the relationship may not have been detected in H I due to removal of a large number of scans, reducing the net exposure times for those objects.

Figure 3 displays the relationship between the H I gas mass to blue light ratio and the blue luminosity for the 25 IEG (green) and ETG comparison (purple) samples. The IEG sample adds data to the sparsely-populated low-luminosity end of this relation. The relationship indicates that lower luminosity galaxies are generally more gas-rich (higher M_{HI}/L_B). While the IEGs fall almost completely within the locus of points defined by the comparison sample, the IEGs with detected H I appear to hug the upper envelope. A possible flattening in the upper envelope at $M_B \lesssim -16.6$ is suggested, the existence of which could be bolstered by additional low luminosity galaxy observations.

Kernel density estimations⁴ (KDE) of the $\log(M_{\text{HI}}/L_B)$ distributions for the IEG and comparison samples are also displayed in Figure 3. The distribution functions exclude upper limits and data for galaxies with H I fluxes fainter than $0.28 \text{ Jy km s}^{-1}$, the smallest flux among our 14 H I detections. This threshold H I flux criterion removed one of the IEG galaxies, S1323 (Most et al. 2013), from the analysis. The large offset between the two density functions imply a systematic H I gas-richness enhancement (~ 0.6 dex in $\log(M_{\text{HI}}/L_B)$) of IEGs relative to luminosity-matched galaxies in the comparison sample.

4.3. Statistical Analyses

In order to quantify the statistical significance of the possible gas enhancement of the IEGs, a two-sample Anderson–Darling (A–D) test⁵ was applied to a subset of the data used for the density functions in Figure 3. While the IEG H I sample reflects a large range of physical distances (25–127 Mpc; see Equation 1) and blue luminosities ($0.7–234 \times 10^8$), the process of selecting targets having predicted H I fluxes sufficiently high to obtain a 5σ detection within ~ 10 hour exposure may have inadvertently biased the IEG sample to higher M_{HI}/L_B values. One reassuring attribute of Figure 3 that argues against the existence of such a bias is the fact that all

five of the IEG observations conducted by other surveys also lay along the upper envelope in the $\log(M_{\text{HI}}/L_B)$ relation. Nevertheless, to insure that statistical comparisons between the samples are not affected by differing observational flux limits, galaxies having H I fluxes less than $0.28 \text{ Jy km s}^{-1}$ are excluded from the A–D test, reducing the IEG and comparison sample sizes to 18 and 74, respectively. The A–D analysis rejects the null hypothesis that the IEG and the comparison sample are drawn from the same parent population with a p-value of 1×10^{-6} .

The A–D test compares the two samples without regard for the relationship between M_{HI}/L_B and M_B . Figure 3 suggests that lower gas-to-luminosity ratios are associated with galaxies of higher B luminosities, the same end of the plot heavily represented by the comparison sample. To ensure that the A–D statistic is not at least in part driven by the comparison sample’s M_B distribution being significantly weighted towards higher luminosities, multiple linear regression (MLR)⁶ was applied to the same data subset used for the A–D test, shown in Figure 4.

Applying standard techniques (see Appendix B), a 1st-order MLR model adequately fits the data. In this model, $\log(M_{\text{HI}})$ is the dependent variable while M_B and the binary IEG/comparison sample identifier are the independent variables. The linear model is shown in Figure 4 with the 95% confidence intervals.

The interaction between M_B and the sample indicator variable is not significant and it was removed from the model. The non-significance of the interaction term (p-value = 0.4) indicates that the difference between the slopes of the fitted lines for the two samples is not statistically significant. Consequently, both slopes in Figure 4 are equal. However, the sample indicator variable is significant with a p-value of 4×10^{-5} , which indicates that the vertical offset between the two lines is statistically significant. The coefficient for the indicator variable (0.6) represents the magnitude of this offset while controlling for M_B . Because biases potentially exist when comparing the single-dish observations of the IEGs to the mixed single-dish and interferometric data of the comparison sample, MLR analysis was repeated on the subset of comparison data from only single-dish observations, with results indistinguishable from those described above. The statistical analysis indicates that for a given luminosity, IEGs are significantly more gas enhanced than their counterparts in the comparison sample.

⁴ using the `density` function in the `stats` v3.5.1 R package, with a Gaussian kernel and bandwidth set to `bw.nrd0` (e.g., Silverman’s rule of thumb).

⁵ using the `ad.test` function in the `kSample` R package Scholz & Zhu (2018)

⁶ using the `lm` function in the `stats` R package

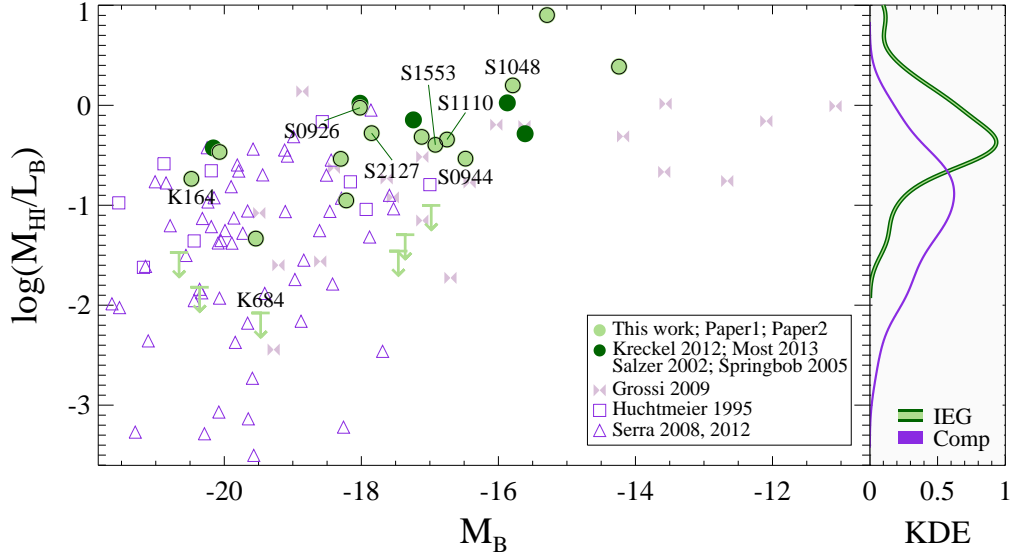


Figure 3. **Left panel:** The log of the H I mass-to-blue luminosity ratio vs. absolute blue magnitude for the IEG and comparison samples. The same color coding is used as in Figure 2. **Right panel:** The kernel distribution estimation of the IEG (green) and comparison (purple) $\log(M_{\text{HI}}/L_B)$ distributions. This analysis includes only those galaxies having measured H I fluxes ($S_{\text{HI}} \geq 0.28 \text{ Jy km s}^{-1}$) that would have been detectable by our survey constraints. An offset between the IEG and comparison sample distributions is apparent.

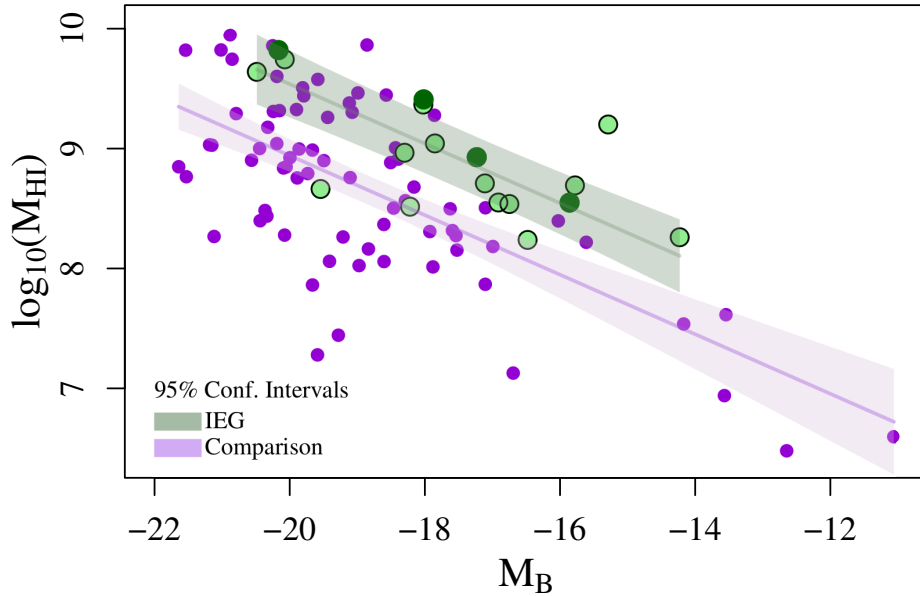


Figure 4. Statistical analyses: The log of the H I-mass vs. absolute blue magnitude with same color legend as Figure 2 and displaying the same dataset used to construct the KDEs displayed in Figure 3, e.g. those galaxies having $S_{\text{HI}} \geq 0.28 \text{ Jy km s}^{-1}$ for statistical analysis having the same color legend as Figure 3. The fitted lines display the results of linear regression analysis; shaded regions are the 95% confidence intervals for the IEG and comparison samples. The analysis supports the hypothesis that the H I mass distributions of the two samples are distinct.

The MLR analysis supports the A–D test results that the ~ 0.6 dex vertical ($\log(M_B)$) displacement between the two samples is statistically significant. However, the systematic H I gas enhancement of the IEG sample appears to have statistical significance only when considered with respect to luminosity. When MLR analysis is applied using color ($B-V$) instead of M_B as an independent variable, the IEG and comparison samples are statistically indistinguishable in Figure 2. In other words, the IEGs do not appear to be gas enhanced relative to comparison galaxies of similar optical color but are gas enriched when compared to galaxies of similar luminosity.

Other authors have found galaxies in loose groups, the field and cluster outskirts to have higher overall H I mass-to-light ratios relative to ETGs in dense environments. Some have suggested this finding supports the emergence of early-type morphology via pre-processing inside galaxy groups (Serra et al. 2012) or of gas accretion from the intergalactic medium (Grossi et al. 2009; Kereš et al. 2005; Macciò et al. 2006). The degree of H I enhancement of ETGs in extremely isolated environments relative to field and loose group members is an unanticipated finding and one not previously explored, to our knowledge, in systems as isolated as the IEG sample. The systematic H I enhancement seen in the IEGs potentially provide a valuable clue in the understanding of ETG formation in low density environments, but exercising some caution in over-interpretation of the statistical analysis is prudent given the small IEG sample size. If the enhancement is real, the origin of the excess gas is of interest. The gas could reflect an unusually low gas consumption rate in the galaxies’ early history, potentially a unique feature of extremely isolated systems. The lack of enhancement in the comparison galaxies could be the result of neutral gas “hidden” in a different gas phase or of H I lost to interactions with higher density environments such as those of loose groups.

5. CONCLUSIONS

Seven of the eight IEGs presented in this study have detectable H I emission. Adding these systems to those presented in Papers 1 & 2 and data from the literature for five other IEGs from other surveys, emission is detected in 19 of the 25 IEGs or about 76% of the sample.

Five of the galaxies presented as the targets of new observations in this paper have Gaussian-like H I profiles. Serra et al. (2012) find that a majority of ETGs in low density environments with detectable H I have regularly rotating gaseous disks or rings, suggesting that the detected H I gas in these five galaxies is likely in

disks which are either face-on or have near solid-body rotation and centrally-peaked radial gas density profiles characteristic of dwarf galaxies. Over half (8 of the 14 detected IEGs) of the total H I IEG sample presented here and in Papers 1 & 2 have Gaussian-like H I profiles. Of the other IEGs detected in H I, 4 have two H I peaks, 1 has a plateau or rectangular profile shape, and 1 has three H I peaks.

We have compared the H I gas-richness of our consolidated study of 25 IEGs to a comparison ETG sample drawn from Huchtmeier et al. (1995), Grossi et al. (2009), and Serra et al. (2012, 2008) consisting largely of loose group members. Across both samples, bluer ETGs are generally more gas-rich. The IEG sample increases the sample coverage at the blue end of that relationship. We also find that the low luminosity galaxies (dwarfs) in the IEG sample are more gas-rich, consistent with the ETG comparison sample. Our study improves the coverage of this relationship at the sparsely populated low-luminosity end and finds that gas-richness is dramatically different between the comparison sample and the significantly more isolated IEGs. Across ~ 2 orders of magnitude in luminosity, the IEGs are found to have, with a high level of statistical significance, gas masses that are systematically higher than those of galaxies of similar luminosity in the ETG comparison sample. Of particular note is that the IEG gas enrichment is seen not only in the blue “dwarf”-like galaxies but also in the luminous red objects in the sample.

Other studies assessing the role of environment on the gas-richness of ETGs in the field, in loose groups and in the outskirts of clusters have concluded that such objects are generally more gas-rich than their cluster counterparts (di Serego Alighieri et al. 2007; Grossi et al. 2009; Serra et al. 2012). The significant neutral gas enhancement of the isolated ETGs relative to the low density comparison sample may suggest that ETG mass assembly continues or that the gas of ETGs is retained in the absence of a galaxy group environment (Serra et al. 2012). While some of the IEGs exhibit low surface brightness morphological evidence for past merging events in the optical bands pointing to a potential source of the H I gas and highly asymmetric features found in their H I line profiles, other systems may represent early-type galaxies that are continuing to assemble via quiescent H I accretion from the cosmic web.

T.A. is funded by an appointment to the NASA Postdoctoral Program at the NASA Ames Research Center, administered by Universities Space Research Association under contract with NASA. The Green Bank Observatory is a facility of the National Science Founda-

tion operated under cooperative agreement by Associated Universities, Inc. This research has made use of the NASA/IPAC Extragalactic Database (NED), which is operated by the Jet Propulsion Laboratory, California Institute of Technology, under contract with the National Aeronautics and Space Administration.

REFERENCES

- Aars, C. E., Marcum, P. M., & Fanelli, M. N. 2001, *AJ*, 122, 2923
- Abazajian, K. N., Adelman-McCarthy, J. K., Agüeros, M. A., et al. 2009, *ApJS*, 182, 543
- Ashley, T., Marcum, P. M., & Fanelli, M. N. 2017, *AJ*, 153, 158
- . 2018, *AJ*, 155, 15
- Barnes, J. E. 2002, *MNRAS*, 333, 481
- Bruzual, G., & Charlot, S. 2003, *MNRAS*, 344, 1000
- Cook, D. O., Dale, D. A., Johnson, B. D., et al. 2014, *MNRAS*, 445, 890
- di Serego Alighieri, S., Gavazzi, G., Giovanardi, C., et al. 2007, *A&A*, 474, 851
- Duc, P.-A., Brinks, E., Wink, J. E., & Mirabel, I. F. 1997, *A&A*, 553, 537
- Fuse, C., Marcum, P., & Fanelli, M. 2012, *AJ*, 144, 57
- Grossi, M., di Serego Alighieri, S., Giovanardi, C., et al. 2009, *A&A*, 498, 407
- Gunn, J. E., & Gott, J. Richard, I. 1972, *ApJ*, 176, 1
- Haynes, M. P., Giovanelli, R., Martin, A. M., et al. 2011, *AJ*, 142, 170
- Huchtmeier, W. K., Sage, L. J., & Henkel, C. 1995, *A&A*, 300, 675
- Karachentseva, V. E. 1973, *Astrof. Issledovanija Byu. Spec. Ast. Obs.*, 8, 3
- Kereš, D., Katz, N., Weinberg, D. H., & Davé, R. 2005, *MNRAS*, 363, 2
- Kreckel, K., Platen, E., Aragón-Calvo, M. A., et al. 2012, *AJ*, 144, 16
- Larson, R. B., Tinsley, B. M., & Caldwell, C. N. 1980, *ApJ*, 237, 692
- Lokas, E. L., Ebrova, I., Pino, A. d., et al. 2016, *ApJ*, 826, 227
- Maccio, A. V., Moore, B., Stadel, J., & Diemand, J. 2006, *MNRAS*, 366, 1529
- Marcum, P. M., Aars, C. E., & Fanelli, M. N. 2004, *AJ*, 127, 3213
- Mihos, J. C. 2001, *ApJ*, 550, 94
- Moore, B., Lake, G., Quinn, T., & Stadel, J. 1999, *MNRAS*, 304, 465
- Morganti, R., De Zeeuw, P. T., Oosterloo, T. A., et al. 2006, *MNRAS*, 371, 157
- Most, H. P., Cannon, J. M., Salzer, J. J., et al. 2013, *AJ*, 145, 150
- Naab, T., Johansson, P. H., Ostriker, J. P., & Efstathiou, G. 2007, *ApJ*, 658, 710
- Niemi, S.-M., Heinamaki, P., Nurmi, P., & Saar, E. 2010, *MNRAS*, 405, 477
- Oosterloo, T., Morganti, R., Crocker, A., et al. 2010, *MNRAS*, 409, 500
- Salzer, J. J., Rosenberg, J. L., Weisstein, E. W., Mazzarella, J. M., & Bothun, G. D. 2002, *AJ*, 124, 191
- Schlafly, E. F., & Finkbeiner, D. P. 2011, *ApJ*, 737, 103
- Scholz, F., & Zhu, A. 2018, *kSamples: K-Sample Rank Tests and their Combinations*. R package version 1.2-8, <https://cran.r-project.org/package=kSamples>, ,
- Serra, P., Trager, S. C., Oosterloo, T. A., & Morganti, R. 2008, *A&A*, 483, 57
- Serra, P., Oosterloo, T., Morganti, R., et al. 2012, *MNRAS*, 422, 1835
- Springob, C. M., Haynes, M. P., Giovanelli, R., & Kent, B. R. 2005, *ApJS*, 160, 149
- van Driel, W., & van Woerden, H. 1991, *A&A*, 243, 71
- Willmer, C. N. A. 2018, *ApJS*, 236, 47

APPENDIX

A. STANDARDIZATION OF COMPARISON SAMPLE DATA

The “standardized” data used for the comparison sample in this paper is presented in Table A1. For details regarding the standardization process, see Section 3.1.

Table A1. Comparison Galaxy H I and Optical Photometry

Name	RA (2000)	Dec (2000)	Distance	M_B	B–V	S_{HI}	M_{HI}	$\log_{10}(M_{\text{HI}}/L_B)$	Source
	(hh mm ss.s)	(dd mm ss)	(Mpc)	(mag)	(mag)	(Jy km s ⁻¹)	(10 ⁸ M _⊙)	(M _⊙ /L _⊙)	
(1)	(2)	(3)	(4)	(5)	(6)	(7)	(8)	(9)	(10)
UGC1503	02 01 19.88	+33 19 47.19	71	-20.2	0.82	3.30	39.5	-0.65	2
N807	02 04 55.66	+28 59 14.79	66	-20.9	0.88	8.40	87.7	-0.58	2
N855	02 14 03.49	+27 52 38.42	10	-17.0	0.65	6.20	1.5	-0.79	2
N1023	02 40 24.00	+39 03 47.82	11	-20.2	0.95	67.06	20.5	-0.92	3
N1490	03 53 34.22	-66 01 05.01	70	-21.0	...	5.70	65.5	-0.76	4
N1947	05 26 47.61	-63 45 36.10	12	-19.0	0.96	3.00	1.1	-1.74	4
UGC3960	07 40 22.74	+23 16 29.98	32	-18.4	0.79	0.24	0.6	-1.79	3
N2534	08 12 54.15	+55 40 19.43	50	-20.0	0.72	1.40	8.3	-1.25	4
N2594	08 27 17.16	+25 52 43.73	34	-18.5 ^a	0.84	2.80	7.6	-0.70	3
UGC4599	08 47 41.69	+13 25 08.83	29	-18.9	0.82	35.34	72.1	+0.14	1
N2685	08 55 34.71	+58 44 03.83	16	-19.1	0.82	32.48	19.9	-0.51	3
N2764	09 08 17.46	+21 26 36.02	38	-19.4	0.73	5.15	18.0	-0.70	3
N2768	09 11 37.50	+60 02 14.00	23	-21.1	0.93	1.50	1.8	-2.36	4
N2824	09 19 02.23	+26 16 11.93	40	-18.9	0.87	0.10	0.4	-2.16	3
N2810	09 22 04.49	+71 50 38.46	53	-20.6	0.97	1.20	7.9	-1.50	4
N2859	09 24 18.53	+34 30 48.55	26	-20.3	0.91	1.68	2.7	-1.88	3
Mrk706	09 34 03.03	+11 00 21.73	35	-17.5	0.60	0.64	1.9	-0.92	1
SDSSJ093608.59+061525.4	09 36 08.59	+06 15 25.42	34	-15.6 ^a	0.54	0.60	1.6	-0.21	1
N2962	09 40 53.93	+05 09 56.92	28	-19.5	0.98	4.22	7.9	-1.08	1
N2974	09 42 33.28	-03 41 56.90	26	-20.4	0.95	5.98	9.9	-1.36	2
N3032	09 52 08.15	+29 14 10.36	25	-18.8	0.66	1.01	1.4	-1.55	3
CGCG064-021	09 59 43.48	+11 39 38.68	40	-18.6 ^a	0.79	0.30	1.1	-1.56	1
N3073	10 00 52.07	+55 37 07.79	20	-17.5	0.65	1.43	1.4	-1.04	3
N3108	10 02 29.02	-31 40 38.70	35	-20.2	0.96	6.90	20.2	-0.97	4
UGC5408	10 03 51.87	+59 26 10.27	45	-18.5	0.56	0.67	3.2	-1.06	3
N3182	10 19 33.02	+58 12 20.61	33	-19.7	0.94	0.03	7.9E-02	-3.14	3
ESO092-21	10 21 05.52	-66 29 31.40	25	-19.0	...	19.20	28.8	-0.31	4
N3265	10 31 06.77	+28 47 48.01	22	-17.9	0.73	1.77	2.0	-1.04	2
N3384	10 48 16.88	+12 37 45.38	12	-19.6	0.91	0.59	0.2	-2.73	3
SDSSJ104926.70+121528.0	10 49 26.70	+12 15 28.01	22	-14.2 ^a	0.45	0.31	0.3	-0.31	1
N3414	10 51 16.20	+27 58 30.36	24	-20.1	0.95	1.35	1.9	-1.93	3
SDSSJ105131.35+140653.2	10 51 31.34	+14 06 53.17	12	-12.1 ^a	0.69	0.22	7.1E-02	-0.16	1
N3457	10 54 48.63	+17 37 16.46	19	-17.9	0.77	1.23	1.0	-1.32	3
N3489	11 00 18.57	+13 54 04.40	12	-19.3	0.82	0.86	0.3	-2.44	1
N3499	11 03 11.03	+56 13 18.19	26	-17.7	0.94	0.04	6.2E-02	-2.46	3

Table A1 continued

Table A1 (continued)

Name	RA (2000)	Dec (2000)	Distance	M_B	B-V	S_{HI}	M_{HI}	$\log_{10}(M_{HI}/L_B)$	Source
	(hh mm ss.s)	(dd mm ss)	(Mpc)	(mag)	(mag)	(Jy km s ⁻¹)	(10 ⁸ M _⊙)	(M _⊙ /L _⊙)	
(1)	(2)	(3)	(4)	(5)	(6)	(7)	(8)	(9)	(10)
N3522	11 06 40.46	+20 05 08.00	21	-17.6	0.74	1.92	2.1	-0.90	3
UGC6176	11 07 24.68	+21 39 25.53	39	-18.4	0.92	2.76	10.1	-0.55	3
IC676	11 12 39.81	+09 03 21.03	24	-19.2	0.77	1.33	1.8	-1.60	1
SDSSJ111445.02+123851.7	11 14 45.02	+12 38 51.71	5	-11.1 ^b	0.38	0.62	4.0E-02	-0.01	1
N3608	11 16 58.95	+18 08 55.26	22	-20.1	0.92	0.12	0.1	-3.07	3
IC2684	11 17 01.04	+13 05 58.70	5	-12.7 ^a	0.55	0.57	3.0E-02	-0.76	1
SDSSJ111701.18+043944.2	11 17 01.17	+04 39 44.21	24	-13.6 ^a	0.44	0.30	0.4	+0.02	1
N3619	11 19 21.55	+57 45 28.16	26	-19.7	0.93	5.90	9.6	-1.06	3
N3626	11 20 03.81	+18 21 24.62	26	-20.3	0.80	9.71	14.9	-1.13	3
IC692	11 25 53.47	+09 59 14.95	19	-17.1	0.31	3.59	3.2	-0.52	1
N3773	11 38 12.87	+12 06 43.37	10	-17.1	0.34	3.06	0.7	-1.15	1
IC719	11 40 18.50	+09 00 35.59	29	-18.4	0.89	4.08	8.1	-0.63	1
UGC6655	11 41 50.64	+15 58 25.50	5	-13.6	0.48	1.26	8.7E-02	-0.67	1
2MASXJ11434609+1342273	11 43 46.11	+13 42 27.26	42	-16.4 ^a	1.08	0.22	0.9	-0.77	1
N3838	11 44 13.75	+57 56 53.61	23	-18.6	0.90	1.84	2.3	-1.25	3
2MASXJ11460404+1134529	11 46 04.05	+11 34 52.71	43	-17.6 ^a	0.52	0.72	3.1	-0.73	1
N3928	11 51 47.62	+48 40 59.28	18	-18.2	0.65	6.00	4.7	-0.77	2
N3941	11 52 55.36	+36 59 10.78	16	-19.9	0.89	16.07	9.8	-1.13	3
N3945	11 53 13.72	+60 40 32.00	23	-20.1	0.93	5.57	6.8	-1.38	3
N3998	11 57 56.13	+55 27 12.92	19	-19.9	0.94	6.36	5.7	-1.38	3
N4026	11 59 25.19	+50 57 42.09	18	-19.7	0.90	7.69	6.1	-1.28	3
N4036	12 01 26.75	+61 53 44.80	24	-20.4	0.89	1.80	2.5	-1.95	3
N4111	12 07 03.13	+43 03 56.59	14	-19.1	0.88	12.83	5.7	-1.06	3
N4125	12 08 06.02	+65 10 26.90	24	-21.3	0.91	0.20	0.3	-3.27	4
N4150	12 10 33.65	+30 24 05.49	13	-18.3	0.78	0.04	1.8E-02	-3.22	3
N4203	12 15 05.05	+33 11 50.37	20	-19.8	0.93	27.70	27.2	-0.66	3
N4278	12 20 06.82	+29 16 50.72	16	-20.1	0.90	11.40	7.0	-1.35	4
N4521	12 32 47.65	+63 56 21.13	39	-19.8	0.88	0.15	0.5	-2.37	3
ESO381-47	13 01 05.39	-35 36 59.59	65	-20.2	...	7.10	71.0	-0.42	4
IC4200	13 09 34.76	-51 58 06.89	52	-20.8	...	8.70	54.9	-0.78	4
N5018	13 13 01.03	-19 31 05.49	40	-21.6	0.84	1.90	7.0	-1.99	4
N5103	13 20 30.07	+43 05 02.30	23	-18.3	0.81	2.88	3.7	-0.93	3
N5173	13 28 25.27	+46 35 29.93	38	-19.9	0.85	6.14	20.9	-0.81	3
N5198	13 30 11.40	+46 40 14.79	39	-20.4	0.91	0.84	3.0	-1.84	3
N5338	13 53 26.55	+05 12 27.95	10	-16.7	0.61	0.57	0.1	-1.73	1
N5422	14 00 42.03	+55 09 52.10	30	-19.7	0.94	0.33	0.7	-2.18	3
N5557	14 18 25.72	+36 29 36.81	48	-21.5	0.90	1.05	5.8	-2.02	3
N5582	14 20 43.12	+39 41 36.90	25	-19.6	0.86	24.67	37.3	-0.44	3
N5631	14 26 33.29	+56 34 57.46	32	-20.2	0.90	4.51	10.9	-1.21	3
SDSSJ144329.18+043153.4	14 43 29.18	+04 31 53.41	28	-16.0 ^a	0.50	1.36	2.5	-0.19	1
UGC9519	14 46 21.08	+34 22 14.00	28	-17.9	0.98	10.36	18.8	-0.05	3
N5866	15 06 29.49	+55 45 47.57	16	-20.3	0.84	0.17	0.1	-3.29	3
N5903	15 18 36.52	-24 04 06.89	36	-21.1	0.88	3.40	10.6	-1.61	4
ESO140-31	18 37 53.62	-57 36 39.90	42	-19.8	...	7.70	31.8	-0.60	4

Table A1 continued

Table A1 (*continued*)

Name	RA (2000)	Dec (2000)	Distance	M_B	B-V	S_{HI}	M_{HI}	$\log_{10}(M_{\text{HI}}/L_B)$	Source
	(hh mm ss.s)	(dd mm ss)	(Mpc)	(mag)	(mag)	(Jy km s ⁻¹)	(10 ⁸ M _⊙)	(M _⊙ /L _⊙)	
(1)	(2)	(3)	(4)	(5)	(6)	(7)	(8)	(9)	(10)
N6798	19 24 03.17	+53 37 29.20	37	-19.1	...	7.23	23.7	-0.45	3
IC4889	19 45 15.14	-54 20 38.90	34	-20.8	0.90	7.10	19.4	-1.20	4
N7052	21 18 33.04	+26 26 49.29	67	-21.2	...	1.00	10.7	-1.62	2
N7280	22 26 27.58	+16 08 53.59	28	-19.4	0.87	0.63	1.1	-1.88	3
N7332	22 37 24.54	+23 47 53.99	20	-19.6	0.88	0.04	3.2E-02	-3.50	3
N7426	22 56 02.85	+36 21 40.90	76	-21.5	...	4.80	65.3	-0.98	2
N7468	23 02 59.25	+16 36 18.88	31	-18.6	0.39	12.50	27.6	-0.16	2

NOTE—Column: (1) Designation taken from the Catalog of Isolated Galaxies (?) or the Sloan Digital Sky Survey (Abazajian et al. 2009), respectively. (2)-(3) Galaxy coordinates sourced from the NASA/IPAC Extragalactic Database (NED). (4) Adopted distance (corrected for Virgo Infall). (5)-(6) Absolute B-band magnitude and B-V color, extinction corrected using Schlafly & Finkbeiner (2011). (7) H I flux density integrated over channels with detected emission. (8) Derived H I mass. (9) H I mass-to-blue luminosity ratio in solar units, using an absolute solar luminosity $M_{\odot,B} = 5.44$ (Willmer 2018). (10) Data source: 1–Grossi et al. (2009); 2–Huchtmeier et al. (1995); 3–Serra et al. (2012); 4–Serra et al. (2008)

^aPhotometry derived through transformation of NSA `Sersic flux` data; see Section 3.1 for details.

^bGalaxy not in the NSA; photometry derived by transforming SDSS `Cmodel` magnitudes listed in NED.

B. DETAILS OF STATISTICAL ANALYSIS

To determine whether the offset between the IEG and comparison samples in the M_B and $\log(M_{HI})$ (or equivalently $\log(M_{HI}/L_B)$) relationship is statistically significant, various multiple linear regression models were fit to the data. The `lm` function in the `stats` v3.5.1 R package was used to perform the modeling. Independent modeling to confirm the results and interpretation was performed by one of us (J.D.F.) using `Minitab` statistical software. In these models, M_B is the dependent variable. Independent variables are M_B and a binary indicator variable identifying the sample (e.g., 1 and 0 for IEG and comparison sample, respectively) associated with each observation. Interaction terms and a second-order term for M_B were tried. Equation B1 illustrates a general model:

$$\log(M_{HI}) = \beta_0 + \beta_1 M_{Bc} + \beta_2 S + \beta_3 S M_{Bc} + \beta_4 M_{Bc}^2 + \beta_5 S M_{Bc}^2 \quad (\text{B1})$$

where β_0 is the constant, M_{Bc} is a “centered” variable, β_i are coefficients, and S identifies the sample.

M_B was centered (mean value was subtracted) to reduce the multicollinearity that the interaction and 2nd-order terms would otherwise produce. Excessive levels of multicollinearity can hamper model selection by producing unstable coefficient estimates, reducing statistical power, and affecting p-values. Variance Inflation Factors (VIFs) were assessed to ensure that problematic amounts of multicollinearity were not present. VIFs were computed using the `vif` function in the `car` R library. VIFs less than ~ 5 indicate that multicollinearity is at an acceptable level. In the models for $\log(M_{HI})$, VIFs associated with the interaction and 2nd-order terms were found to have, at most, values less than 3.5. Additionally, confirmation of normally distributed residuals and of the assumption of homoscedasticity were performed by inspection of residuals, normal Q-Q, and scale-location graphical output of the R `lm` function.

The statistical output includes a p-value for each coefficient that allows one to assess the null hypothesis that the coefficient β_i equals 0. The quadratic terms and interaction terms all had large ($\gtrsim 0.1$) p-values, including β_3 which quantifies the difference between the slopes of the fitted lines for the two samples. Following a standard model reduction process that systematically removes one non-significant term from the model at a time and then re-fits the data, the final model contains M_B and the binary sample indicator variable as the only significant independent variables (see Table A2).

The p-values for all three coefficients are very small. Most notable is the value associated with β_2 , which is the vertical offset in the M_B versus $\log(M_{HI})$ relationship that exists between the IEG and comparison samples (see Figure 4). The corresponding p-value of 4×10^{-5} suggests this offset of 0.6 dex is statistically significant.

Table A2. MLR Results For Final Model

	β_0	β_1	β_2
Value	4.0	-0.25	0.6
Std. Error	0.5	0.03	0.1
p-value	2×10^{-11}	2×10^{-14}	6×10^{-5}

NOTE—Because no interaction and quadratic terms are involved, this model uses M_B rather than the centered variable.